Research Square

Preprints are preliminary reports that have not undergone peer review.
They should not be considered conclusive, used to inform clinical practice,
or referenced by the media as validated information.

Effects of oxide supports and Pt loading on the interfacial structure and catalytic performance of SANIs-inspired catalysts for dry reforming of methane

Chao Hu
Anhui Jianzhu University
Hongye Chen
2973103354@qq.com
Anhui Jianzhu University School of Environment and Energy Engineering https://orcid.org/0009-0005-4178-4379
ZiWen Zhao
Anhui Jianzhu University
Yue Zhang
Anhui Jianzhu University
Rui Zhou
Anhui Jianzhu University
Shenqiao Song
Anhui Jianzhu University
Nai Rong
Anhui Jianzhu University
Xiaokang Wan
Anhui Jianzhu University

Research Article

Keywords: Dry reforming of methane, Metal-support interaction, Interfacial engineering, Pt/NiOx interface, SANIs-inspired catalysts, Ostwald ripening

Posted Date: October 8th, 2026

DOI: https://doi.org/10.21203/rs.3.rs-10741990/v1

License: This work is licensed under a Creative Commons Attribution 4.0 International License.
Read Full License

Effects of oxide supports and Pt loading on the interfacial structure and catalytic performance of SANIs-inspired catalysts for dry reforming of methane

Chao Hu[1*], Hongye Chen[1], Ziwen Zhao[1], Yue Zhang[1], Rui Zhou[1], Shenqiao Song[1], Nai Rong[1], Xiaokang Wan[1]

[1]: School of Environment and Energy Engineering, Anhui Jianzhu University, Hefei 230601, China

*Corresponding author: Chao Hu Tel.: +86 551 63828252

E-mail: chaohu@mail.ustc.edu.cn

Abstract

Catalysts that simultaneously achieve high catalytic activity and strong resistance to sintering are highly desirable for methane dry reforming (DRM), yet the rational design of such catalysts remains challenging. Inspired by the Single-Atom Nano-Islands (SANIs) concept, a series of SANIs-inspired Pt catalysts with oxide-modified SiO_2 supports were rationally designed and synthesized via the liquid-phase electrostatic adsorption method to engineer the metal-support interface. Structural characterization confirmed the successful construction of the SANIs-inspired Pt/NiO_x-SiO_2 catalyst with highly dispersed Pt species and intimate Pt/NiO_x spatial association. Combined X-ray photoelectron spectroscopy and hydrogen temperature-programmed reduction analyses revealed strong metal-support interaction (MSI) at the Pt/NiO_x interface, which was associated with superior DRM performance among the catalysts studied. Further optimization of Pt loading revealed that an appropriate Pt loading was essential for balancing active site availability and interfacial stability. The 4.2wt% Pt/NiO_x-SiO_2 catalyst achieved the optimal interfacial structure, delivering a CH_4 conversion of 85% and retaining a conversion of 81.3% after 200 h of continuous DRM operation. In contrast, excessive Pt loading promoted Pt aggregation and Ostwald ripening under high-temperature DRM conditions, accompanied by NiO_x crystallization and structural redistribution, resulting in Pt/NiO_x interface reconstruction and weakened interfacial interaction. These findings demonstrate that the synergistic regulation of MSI and Pt distribution is critical for achieving highly active and stable DRM catalysts and provide an effective strategy for catalyst design through interfacial structure engineering.

Keywords: Dry reforming of methane; Metal-support interaction; Interfacial engineering; Pt/NiO_x interface; SANIs-inspired catalysts; Ostwald ripening

1 Introduction

Methane dry reforming (DRM) has attracted extensive attention as an effective route for the simultaneous conversion of CH_4 and CO_2 into syngas with high added value. However, the highly endothermic nature of DRM requires severe high-temperature reaction conditions, under which active metal species are prone to migration and aggregation, resulting in catalyst sintering and gradual deactivation [1-3]. Therefore, developing catalysts that can simultaneously achieve high catalytic activity

and excellent thermal stability remains a significant challenge.

Single-atom catalysts have been extensively investigated due to their maximum atomic utilization efficiency and unique electronic properties [4]. Nevertheless, isolated metal atoms often suffer from poor thermal stability under high-temperature reaction conditions because of their strong tendency to migrate and aggregate, leading to the loss of active sites. To address this limitation, Xu Li et al. proposed the concept of Single-Atom Nano-Islands (SANIs), which consist of a high surface area support, oxide nanoclusters, and highly dispersed active metal species [5,6]. The localized metal-oxide interfaces in SANIs can provide strong anchoring effects for active metals and effectively inhibit metal migration and sintering. Moreover, oxide nanoclusters can regulate the electronic structure of active metals through metal-support interactions (MSI), thereby offering an effective strategy for designing thermally stable catalysts [7].

Inspired by the SANIs concept, constructing oxide modified and SiO_2 supported catalysts provides a promising strategy for regulating MSI and improving the thermal stability of active metals. In these catalysts, oxide species act as interfacial regulators that not only provide anchoring sites for metal species but also modulate interfacial charge transfer and electronic structures [7,8]. Previous studies have demonstrated that oxide reducibility, oxygen affinity, and interfacial adhesion energy are closely associated with metal stabilization and catalytic behavior [9-14]. However, the role of different oxide species in modulating MSI and determining the catalytic performance of Pt based DRM catalysts remains to be clarified [15]. Therefore, rational screening of oxide components is necessary to identify suitable oxide species for SANIs-inspired Pt catalysts. In this research, NiO_x, CoO_x, ZnO_x, CrO_x, and AlO_x were selected as oxide modifiers to construct a series of SANIs-inspired Pt catalysts. By comparing the catalytic performance and interfacial properties of these catalysts, the relationship between oxide species, MSI strength, and DRM performance can be elucidated.

Although appropriate oxide selection is essential for constructing efficient Pt based SANIs-inspired catalysts, the long-term stability of these catalysts under high-temperature DRM conditions is also closely related to the dynamic evolution of metal-support interfaces [16-19]. Actually, meta-support interfaces are not static during high-temperature reactions [20]. Under DRM conditions, active metal species may undergo migration, aggregation, and structural reconstruction, which are closely associated with Ostwald ripening processes and ultimately affect catalyst durability [21]. Recent studies have shown

that regulating metal diffusion pathways and interfacial structures can effectively suppress nanoparticle growth and improve thermal stability [22-24]. For example, Huang et al. demonstrated that surface structures of MXene-based catalysts could regulate Pt migration pathways during Ostwald ripening, thereby enhancing sintering resistance [25]. Gan et al. further revealed that modifying support structures could influence metal diffusion behavior and improve catalyst stability [26]. Yu et al. showed that Strong MSI could regulate nanoparticle evolution by controlling Ostwald ripening pathways, highlighting the importance of interfacial structural evolution in determining catalyst stability [27]. Therefore, understanding the influence of active metal distribution and interfacial evolution on catalyst stability is crucial for further optimizing SANIs-inspired DRM catalysts.

Inspired by these findings, SANIs-inspired catalysts provide an ideal platform for investigating the relationship between interfacial structure, MSI regulation, and thermal stability. In particular, the variation of active metal loading may alter the relative distribution between Pt species and oxide nanoclusters, thereby affecting interfacial site density, metal migration behavior, and structural evolution during high-temperature DRM reactions. Therefore, optimizing Pt loading is crucial for balancing catalytic activity and thermal stability.

In this study, a series of SANIs-inspired catalysts containing different oxide nanoclusters were first prepared using the liquid-phase electrostatic adsorption (LEA) method, which is based on the principle of surface electrostatic interactions [28-32]. By introducing different metal oxides to modulate the MSI between Pt and the oxide nanoclusters, the aim was to identify the interfacial structure most conducive to DRM catalytic performance. Subsequently, the Pt loading on the selected oxide systems was further optimized to investigate the influence of interfacial Pt distribution on catalytic activity and thermal stability. By synergistically regulating metal-support interactions and interfacial structure evolution, this study successfully developed DRM catalysts featuring optimized interfacial structures, high activity, and excellent thermal stability.

2 Experimental

2.1 Experimental Materials

Nickel nitrate hexahydrate ($Ni(NO_3)_2 \cdot 6H_2O$, AR), zinc nitrate hexahydrate ($Zn(NO_3)_2 \cdot 6H_2O$, AR),

cobalt nitrate hexahydrate ($Co(NO_3)_2 \cdot 6H_2O$, AR), and hydrochloric acid (HCl, AR) were supplied by Sinopharm Chemical Reagent Co., Ltd. (China). Chromium nitrate nonahydrate ($Cr(NO_3)_3 \cdot 9H_2O$, AR ≥ 99%), aluminum nitrate nonahydrate ($Al(NO_3)_3 \cdot 9H_2O$, AR ≥ 99.99%), ammonia solution ($NH_3 \cdot H_2O$, AR ≥ 99.999%), hydrophilic fumed silica Hydrophilic-300 (SiO_2, AR ≥ 99.8%), and chloroplatinic acid hexahydrate ($H_2PtCl_6 \cdot 6H_2O$, AR, Pt ≥ 37.5%) were obtained from Shanghai Aladdin Biochemical Technology Co., Ltd.. Deionized water used throughout the experiments was produced in house.

2.2 Catalyst Preparation Method

The catalysts were synthesized using a combination of the LEA method and the impregnation method [5]. The preparation procedure mainly involved three steps: (i) fabrication of the SiO_2 support plates, (ii) construction oxide supports, and (iii) deposition of active Pt species onto the supports.

2.2.1 SiO_2 Support Plate

First, 360 mg of fumed SiO_2 powder was added to 100 mL of deionized water and dispersed under continuous stirring. The obtained mixture was then treated ultrasonically to form a stable and homogeneous suspension.

2.2.2 Preparation of Supports

Oxide supports were fabricated via a combination of liquid-phase electrostatic adsorption (LEA) and conventional impregnation [32]. Taking NiO_x-SiO_2 as a representative case, 116.4 mg of $Ni(NO_3)_2 \cdot 6H_2O$ was added to the as-prepared SiO_2 suspension. The pH of the mixture was then adjusted to 7.8 by dropwise addition of ammonia solution, enabling electrostatic adsorption of Ni species onto the SiO_2 surface under alkaline conditions. After adsorption, the suspension was vacuum-filtered to collect the solid residue. The obtained product was dried at 80 °C for 12 h in an oven and then gently ground into fine powder. Subsequently, the powder was calcined in a muffle furnace at 600 °C for 12 h to yield the NiO_x-SiO_2 support. Additional data are provided in Table S1.

2.2.3 Preparation of Precursor Solutions

For the preparation of the 2.1wt% Pt/NiO_x-SiO_2 catalyst, 60 μmol of $H_2PtCl_6 \cdot 6H_2O$ was dissolved in 50 mL of hydrochloric acid solution. The pH of the solution was adjusted to the isoelectric point of the Pt precursor on the NiO_x support (pH = 5.3) [33], thereby obtaining the precursor solution. In this

study, $H_2PtCl_6 \cdot 6H_2O$ was used as the Pt precursor, and the Pt loading was controlled within the range of 0.37-6.3wt%. Additional details are summarized in Table S2.

2.2.4 Loading of Active Pt Species

Pt species were introduced onto the supports through the LEA method. Using Pt/NiO_x-SiO_2 as a representative catalyst, 42 mg of the Pt/NiO_x-SiO_2 support was dispersed in 70 mL of deionized water, followed by ultrasonic treatment to obtain a uniform suspension. The pH of the suspension was subsequently adjusted to 5.3, corresponding to the isoelectric point of the support, by the dropwise addition of hydrochloric acid. The precursor solution prepared in Section 2.2.3 was then continuously introduced into the support suspension over 5 h using a peristaltic pump. After addition, the mixture was further stirred for 5 h to facilitate sufficient adsorption of Pt species onto the support surface. After completion of the adsorption process, the solid product was separated by vacuum filtration and repeatedly washed with deionized water to remove residual Pt ions and other soluble species. The resulting precursor powder was dried at 80 °C for 12 h and subsequently calcined at 600 °C for 12 h to obtain the final Pt/NiO_x-SiO_2 catalyst. Additional preparation details are provided in Table S3.

2.3 Catalyst Testing Conditions

For catalysts containing different oxide supports, the Pt loading was fixed at 2.1wt%, and the samples were denoted as Pt/AlO_x-SiO_2, Pt/CrO_x-SiO_2, Pt/ZnO_x-SiO_2, Pt/NiO_x-SiO_2, and Pt/CoO_x-SiO_2. Catalysts with different Pt contents were labeled as 0.37wt% Pt/NiO_x-SiO_2, 0.74wt% Pt/NiO_x-SiO_2, 4.2wt% Pt/NiO_x-SiO_2, and 6.3wt% Pt_2/NiO_x-SiO_2.

The catalytic activity and stability of the catalysts were evaluated in a fixed-bed quartz reactor with an inner diameter of 8 mm and a length of 500 mm. Catalytic activity tests were first carried out in the temperature range of 650-800 °C. For each experiment, 30 mg of the reduced catalyst was loaded into the reactor. Pure CH_4 and CO_2 were introduced with a molar ratio of 1:1, and the gas hourly space velocity (GHSV) was maintained at 20,000 $mL \cdot g^{-1} \cdot h^{-1}$. To investigate the sintering resistance and long-term stability of the catalysts, the DRM reaction was subsequently performed at 750 °C for 24 h. The outlet gas products were analyzed using a GC9790II gas chromatograph (GC) equipped with both a thermal conductivity detector (TCD) and a flame ionization detector (FID). The conversion rates of CH_4 and CO_2 were calculated according to the following equations:

$$CH_4 conversion(\%) = \frac{F_{CH_4,in} - F_{CH_4,out}}{F_{CH_4,in}} \times 100\% \quad (1)$$

$$CO_2 conversion(\%) = \frac{F_{CO_2,in} - F_{CO_2,out}}{F_{CO_2,in}} \times 100\% \quad (2)$$

$$H_2 / CO = \frac{F_{H_2,out}}{F_{CO,out}} \quad (3)$$

Where F_{in} and F_{out} denote the volumetric flow rates of the corresponding gas component at the inlet and outlet of the reactor, respectively. Fig.1 show the SANIs-inspired catalyst design strategy and the effects of oxide species and Pt loading on interfacial structures is presented.

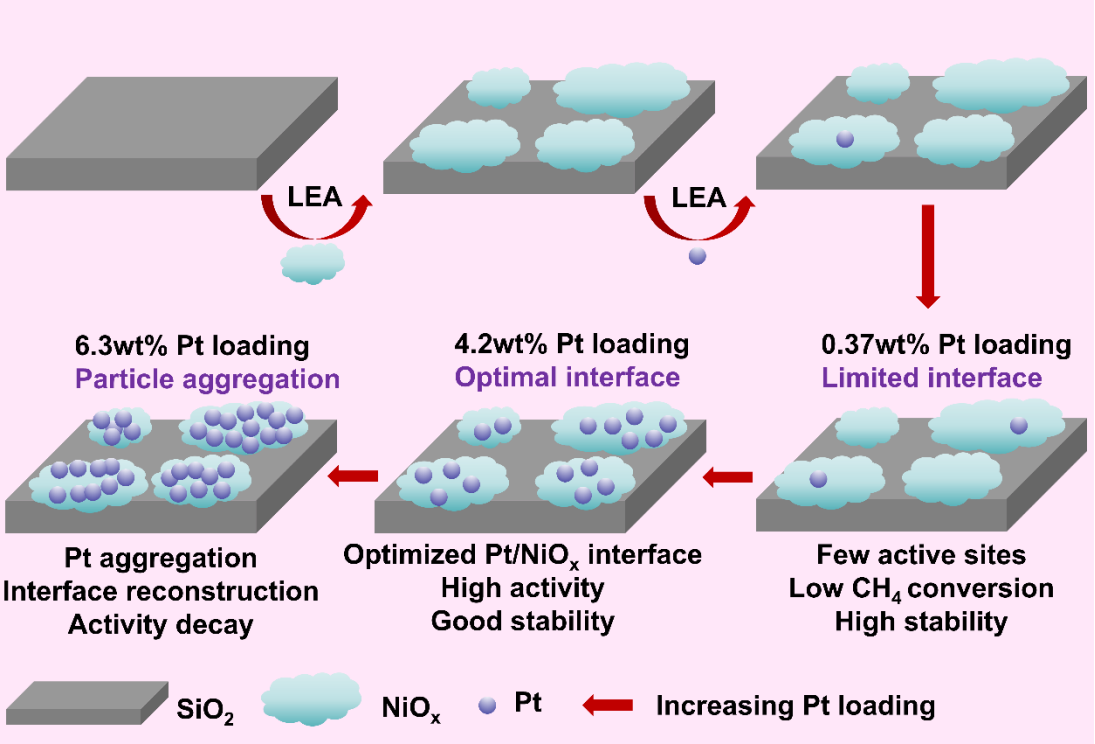


Fig.1 SANIs-inspired Pt catalysts via oxide modification and Pt loading optimization for regulating Pt dispersion, interfacial structure, and DRM performance

3 Results and Discussion

3.1 Catalytic performance and interfacial properties of different oxide-supported catalysts

3.1.1 XPS, DRM, and H_2-TPR characterization of oxide-supported catalysts

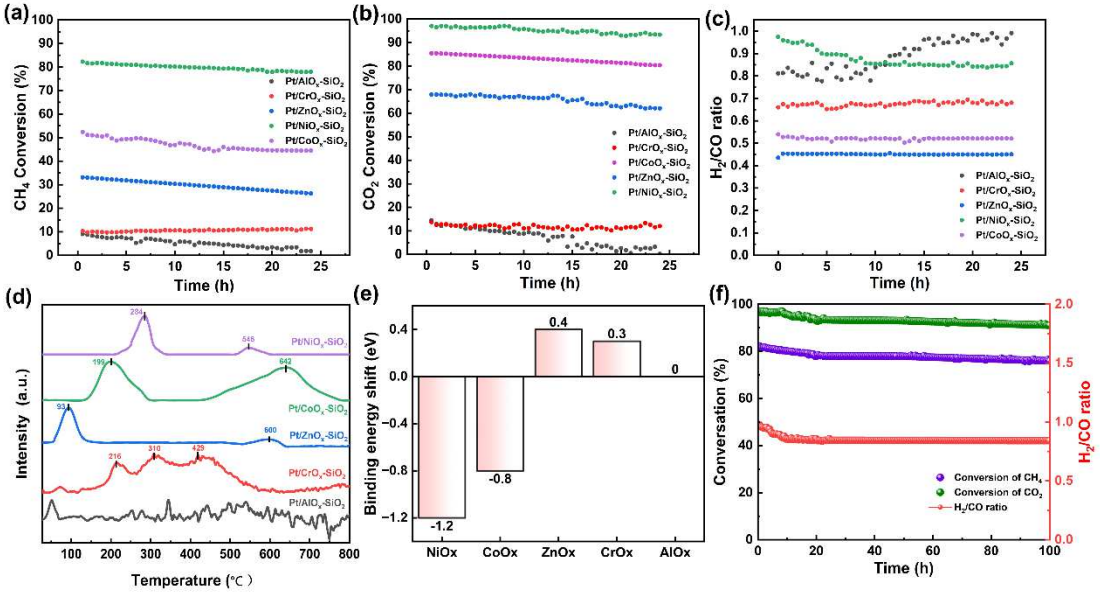


Fig.2 DRM performance, XPS Analysis and H_2-TPR profiles of different oxide-supported catalysts. The DRM reaction conversion rates of the Pt/AlO_x-SiO_2, Pt/CrO_x-SiO_2, Pt/ZnO_x-SiO_2, Pt/NiO_x-SiO_2, and Pt/CoO_x-SiO_2 catalysts for (a) CH_4, (b) CO_2, and (c) H_2/CO; (d)Comparison of H_2-TPR profiles of different oxide-supported catalysts; (e) Comparison of binding energy shifts of different oxide species relative to their standard oxide references; (f) CH_4 conversion, CO_2 conversion and H_2/CO ratio of Pt/NiO_x-SiO_2 for 100 h DRM reaction at 750 °C

XPS was employed to investigate Pt catalysts supported on different metal oxides, and the interfacial electronic interactions between Pt and the oxide supports were systematically analysed. Because the Pt loading in the catalysts supported on different metal oxides is only 2.1wt% and the Pt species are highly dispersed, the Pt 4f signal is relatively weak in some samples. Consequently, the MSI between Pt and various oxide supports were primarily evaluated based on shifts in the oxide-related binding energies. Fig. S1a-S5a show the fitted XPS spectra of Ni 2p, Co 2p, Zn 2p, Cr 2p, and Al 2p for catalysts supported on different oxides. All oxide species exhibit characteristic oxidation-state peaks, indicating that the oxide phases were successfully dispersed on the support surface. As shown in Fig. 2e, the binding-energy

shifts of different oxide supports relative to previously reported reference values were determined based on the fitted XPS spectra, and the corresponding results are summarized in Table 1 [34-38].

Among the investigated oxide modifiers, NiO_x exhibited the largest negative binding energy shift, while CoO_x also showed a pronounced negative shift. In contrast, ZnO_x and CrO_x displayed slight positive shifts, whereas no appreciable shift was observed for AlO_x. The pronounced negative shift of the NiO_x related signal suggests an increase in the electron density of the NiO_x species, consistent with substantial electronic interaction at the Pt/ NiO_x interface [39, 40]. By comparison, the negligible shift observed for AlO_x suggests a relatively limited electronic interaction between Pt and AlO_x [41, 42]. These results demonstrate that the identity of the oxide modifier influences the interfacial electronic structure of the Pt catalysts. The possible relationships among these electronic interactions, catalyst reducibility, and DRM performance were further examined through H_2-TPR analysis and 24 h stability tests.

Fig. 2(a-b) illustrate the DRM performances of catalysts supported on different metal oxide supports at 750 °C. Among them, the Pt/NiO_x-SiO_2 catalyst delivers the highest activity and stability during the 24 h continuous reaction. The CH_4 and CO_2 conversions decrease by only approximately 4.3% and 3.6%, respectively. These results demonstrate excellent resistance to catalyst sintering under DRM conditions. By comparison, the Pt/CoO_x-SiO_2, Pt/CrO_x-SiO_2, and Pt/ZnO_x-SiO_2 catalysts retain relatively stable reaction behaviors throughout the test. Nevertheless, their catalytic efficiencies remain markedly lower than that of Pt/NiO_x-SiO_2. This result implies that fewer effective interfacial active sites are involved in the DRM process [43]. In contrast, the Pt/AlO_x-SiO_2 catalyst exhibits inferior catalytic activity and stability, which may be associated with the relatively weak MSI between Pt and AlO_x species [44].

Furthermore, the product distribution results presented in Fig. 2c indicate that the Pt/NiO_x-SiO_2 catalyst exhibits the most favorable H_2/CO ratio among the investigated catalysts. This result suggests the effective suppression of undesirable side reactions during the DRM process. These findings further confirm the beneficial effect of Pt/NiO_x interfacial interactions on catalytic activity and reaction selectivity. Fig. 2f further demonstrates the long-term catalytic stability of the Pt/NiO_x-SiO_2 catalyst during the 100 h DRM reaction. After the initial 20 h, the catalyst maintains highly stable catalytic performance, with only slight and gradual decreases in the CH_4 and CO_2 conversion rates. No sudden deactivation is observed throughout the reaction, indicating excellent structural stability under prolonged high-temperature reaction conditions. During the period from 20 to 100 h on stream, only slight decreases

of approximately 2% in CH_4 conversion and 3% in CO_2 conversion are observed, further confirming the excellent stability of the catalyst during the DRM process. These results clearly indicate that the optimized interfacial interactions between Pt species and NiO_x play a crucial role in stabilizing interfacial active sites and suppressing catalyst deactivation under harsh DRM conditions. In addition, the synergistic effect between NiO_x species and Pt active sites makes a significant contribution to the high catalytic activity and excellent long-term stability of the catalyst.

As shown in Fig. 2d, the H_2-TPR profiles reveal marked differences in the reduction behavior of the catalysts containing different oxide modifiers. In particular, Pt/NiO_x-SiO_2 (Fig. S1b) exhibits distinct low-temperature reduction features with substantial H_2 consumption, suggesting that Pt facilitates the reduction of NiO_x through hydrogen spillover. This behavior is consistent with a strong MSI between Pt and NiO_x. In contrast, Pt/CoO_x-SiO_2 (Fig. S2b) exhibits reduction features predominantly in the high-temperature region, indicating the relatively low reducibility of the CoO_x species. Together with its inferior performance in the 24 h stability test, this result suggests that the limited reducibility of CoO_x may restrict the participation of Pt/CoO_x interfacial sites in the DRM reaction [45, 46]. Pt/ZnO_x-SiO_2 (Fig. S3b) displays a broad reduction feature centered at approximately 600 °C and only weak H_2 consumption in the low-temperature region, indicating the relatively low reducibility of ZnO_x and a limited Pt assisted reduction effect. This behavior may reflect relatively weak interactions between Pt and ZnO_x [47]. Pt/CrO_x-SiO_2 (Fig. S4b) exhibits multiple reduction features at 216, 310, and 429 °C, which may be assigned to the stepwise reduction of chromium oxide species in different oxidation states or coordination environments [48]. Finally, Pt/AlO_x-SiO_2 (Fig. S5b) shows no distinct reduction feature within the investigated temperature range, consistent with the poor reducibility of AlO_x. The absence of an appreciable low-temperature reduction feature also suggests a limited Pt assisted reduction effect.

3.1.2 Structural and elemental characterization of the Pt/NiO_x-SiO_2 Catalyst

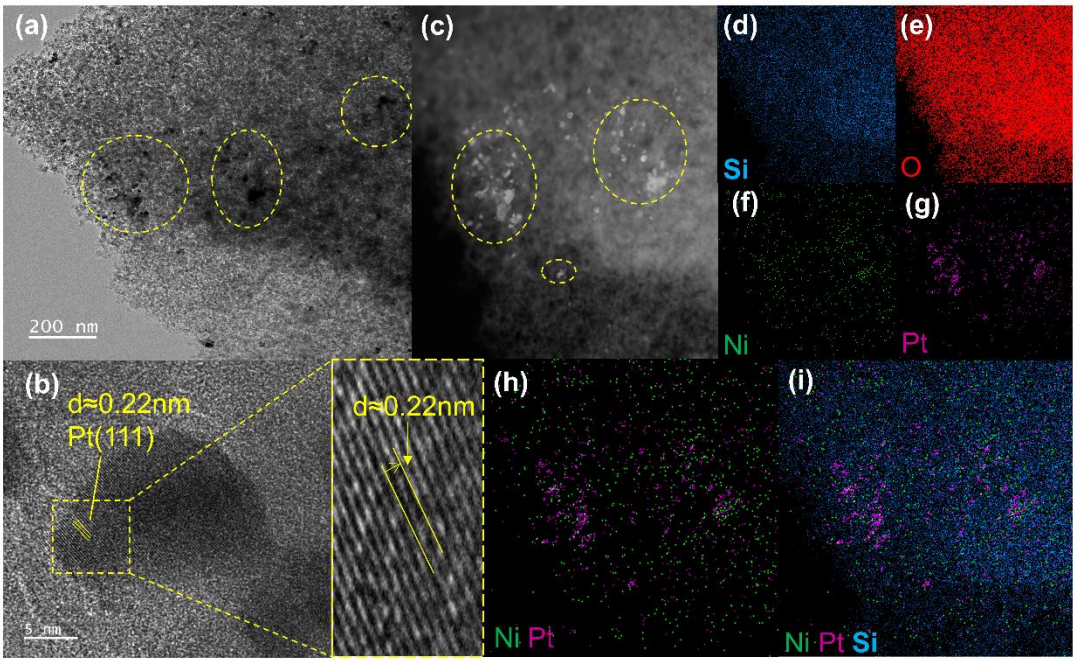


Fig. 3 TEM characterization of Pt/NiO_x-SiO_2 catalyst. (a) TEM image; (b) HRTEM image with enlarged lattice fringe region; (c) HAADF-STEM image; (d-g) STEM-EDS elemental mappings of Si, O, Ni, and Pt; (h) Overlay elemental mapping of Ni and Pt; (i) Overlay elemental mapping of Ni, Pt, and Si

To verify the dispersion state of Pt species and the interfacial structure between Pt and oxide species, Pt/NiO_x-SiO_2 was selected as a representative catalyst and characterized by Transmission Electron Microscopy (TEM), High-Resolution Transmission Electron Microscopy (HRTEM), High-Angle Annular Dark-Field Scanning Transmission Electron Microscopy (HAADF-STEM) and Scanning Transmission Electron Microscopy-Energy Dispersive X-ray Spectroscopy (STEM-EDS). As shown in Fig. 3a, no obvious large Pt particles were observed on the Pt/NiO_x-SiO_2 catalyst, while uniformly distributed nanoscale contrast regions were identified, indicating that the LEA method effectively promoted the dispersion of Pt species. Further HRTEM observation (Fig. 3b) revealed clear lattice fringes with an interplanar spacing of approximately 0.22 nm, which can be assigned to the Pt (111) plane, suggesting the presence of ordered Pt species on the support. Meanwhile, the HAADF-STEM image (Fig. 3c) displayed dispersed bright contrast regions. The corresponding STEM-EDS elemental mappings (Fig. 3(d-i)) demonstrated a spatial correlation between Pt and Ni species, whereas Si was mainly distributed in the support region, suggesting that Pt species were preferentially associated with NiO_x enriched

regions. These results confirm the successful construction of highly dispersed Pt species and Pt/NiO_x interfacial structures via the LEA method.

To exclude the influence of textural properties on the catalytic performance, N_2 adsorption–desorption measurements were further performed to evaluate the specific surface areas of different oxide-supported catalysts. As summarized in Table 1, although Pt/NiO_x-SiO_2 exhibited a relatively higher Brunauer-Emmett-Teller (BET) surface area than the other catalysts, all samples showed comparable surface areas within the range of 250-304 m^2g. Therefore, the significant differences in DRM performance among these catalysts were unlikely to be solely determined by their textural properties, but were mainly associated with the distinct MSI between Pt species and different oxide-supports.

Table 1: Textural properties and binding energy shifts of catalysts with different oxide modifiers

Catalysts	**BET surface** （m^2/g）	**XPS Standard BE (ev)**	**XPS Observed BE (ev)**	**XPS BE Shift (ev)**
Pt/NiO_x-SiO_2	303.96	856.2	855.0	-1.2
Pt/CoO_x-SiO_2	276.26	781.0	780.2	-0.8
Pt/ZnO_x-SiO_2	250.58	1022.2	1022.6	0.4
Pt/CrO_x-SiO_2	269.64	576.2	576.5	0.3
Pt/AlO_x-SiO_2	266.53	74.5	74.5	0

Based on the above results, the Pt/NiO_x-SiO_2 catalyst exhibits the most favorable interfacial electronic interactions and catalytic performance among the catalysts supported on the investigated metal oxides. Significant XPS binding energy shifts and characteristic reduction behavior suggest the presence of strong MSI between Pt and NiO_x species. Therefore, NiO_x supported catalysts were further selected to investigate the influence of Pt loading on the balance among interfacial interactions, Pt dispersion, and catalytic stability.

3.2 Effect of Pt loading on Pt/NiO_x interfacial structure and dry reforming of methane performance

3.2.1 Structural and elemental characterization of the Pt/NiO_x-SiO_2 catalysts with different Pt loadings

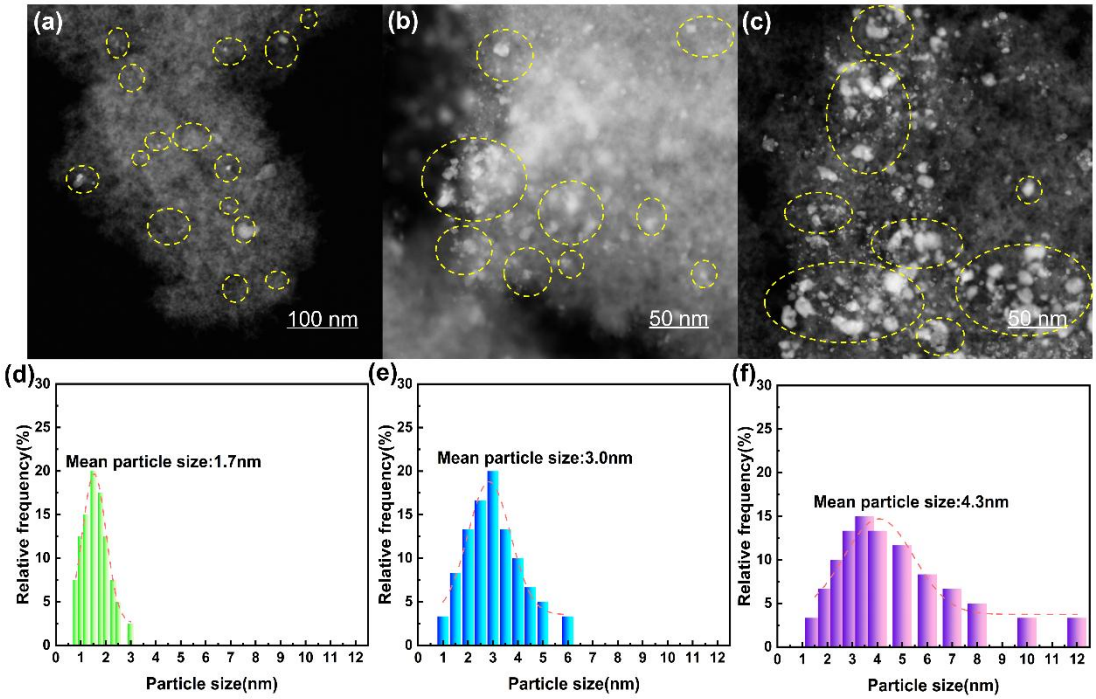


Fig. 4 HAADF-STEM images and corresponding particle size distributions of Pt/NiO_x-SiO_2 catalysts with different Pt loadings. The particle size distribution was obtained by statistically analyzing approximately 50 Pt-containing particles from HAADF-STEM images. (a, d) 0.37wt% Pt/NiO_x-SiO_2; (b, e) 4.2wt% Pt/NiO_x-SiO_2; (c, f) 6.3wt% Pt/NiO_x-SiO_2

To further investigate the effect of Pt loading on the dispersion state of Pt species and the Pt/NiO_x interfacial structure, TEM, HAADF-STEM, and STEM-EDS mapping were performed on Pt/NiO_x-SiO_2 catalysts with different Pt loadings. As shown in Fig. 4(a-c), the distribution characteristics of Pt species on the catalyst surface varied significantly with increasing Pt loading.

As shown in Fig. S6, no obvious large Pt particles were observed in the TEM images of the 0.37wt% Pt/NiO_x-SiO_2 catalyst, and the EDS mapping results revealed a relatively uniform distribution of Pt species, indicating that a low Pt loading was beneficial for maintaining highly dispersed Pt species. Statistical analysis based on HAADF-STEM images further revealed that the Pt species exhibited a

narrow size distribution, with a mean particle size of approximately 1.7 nm (Fig. 4d). However, due to the limited Pt content, the number of Pt species and corresponding Pt/NiO_x interfacial sites was relatively insufficient, which may restrict the availability of active sites during the DRM reaction.

With increasing Pt loading to 4.2wt% (Fig. S7), the Pt-related signals became more pronounced, while no obvious large Pt particles were detected in the HAADF-STEM images. Moreover, the EDS mapping results demonstrated a good spatial correlation between Pt and Ni species, suggesting that an appropriate increase in Pt loading could increase the density of Pt/NiO_x interfacial sites while maintaining favorable Pt dispersion, thereby facilitating the formation of abundant interfacial active structures. The particle size distribution analysis showed that the mean particle size of Pt species increased moderately to approximately 3.0 nm (Fig. 4e), indicating that Pt species remained well dispersed despite the increased loading. This balance between Pt dispersion and interfacial site density may contribute to the superior catalytic performance of the 4.2wt% Pt/NiO_x-SiO_2 catalyst.

When the Pt loading was further increased to 6.3wt% (Fig. S8), the Pt-related signals became further intensified, accompanied by the appearance of locally enriched Pt regions. Meanwhile, the particle size distribution became broader, and the mean particle size increased to approximately 4.3 nm (Fig. 4f), indicating enhanced Pt aggregation at excessive loading. The excessive Pt loading may enhance the interaction among Pt species and promote the migration and aggregation of active metal species under high-temperature DRM conditions, leading to partial loss of Pt/NiO_x interfacial sites and catalyst deactivation.

These results demonstrate that Pt loading plays a critical role in regulating the dispersion state of Pt species and the Pt/NiO_x interfacial structure. An appropriate Pt loading enables a balance between the density of active sites and interfacial structural stability, which is essential for constructing favorable Pt-NiO_x interfacial structures.

XPS was employed to investigate the Pt/NiO_x-SiO_2 catalysts with varying Pt loadings and to examine the effect of Pt loading on the surface chemical states. As shown in Fig. 5a, the Ni species were mainly present as Ni^{2+}. The corresponding satellite peaks further confirmed the existence of Ni^{2+} species, indicating that NiO like structures were dispersed on the SiO_2 support. All catalysts exhibited characteristic Ni^{2+} $2p_{1/2}$ and Ni^{2+} $2p_{3/2}$ peaks at approximately 855 eV and 872 eV, respectively, consistent

with previous reports [49, 50]. Based on the characteristic peak positions, the peak areas and binding energies of Ni^{2+} $2p_{2/3}$ and Ni^{2+} $2p_{1/2}$ were quantitatively analyzed for all catalysts. The results are summarized in Table S4. As shown in Fig. 6b, the Pt species were mainly present as Pt^{2+}, with characteristic Pt^{2+} $4f_{5/2}$ and Pt^{2+} $4f_{7/2}$ peaks at approximately 75.5 eV and 72.3 eV, respectively, consistent with previous reports [51, 52]. A quantitative analysis of the Pt^{2+} $4f_{5/2}$ and Pt^{2+} $4f_{7/2}$ peak areas and binding energies was also performed for all catalysts. The results are summarized in Table S5.

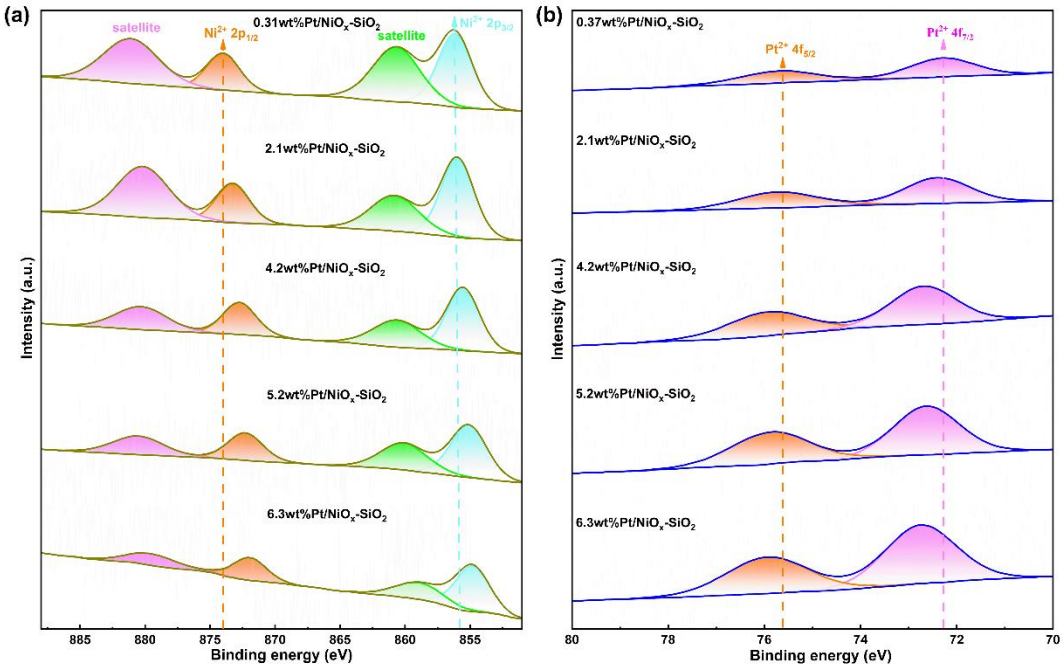


Fig. 5 XPS analysis of Pt/NiO_x-SiO_2 with different Pt loadings. Fitting parameters of (a) Ni 2p and (b) Pt 4f XPS spectra for Pt/NiO_x-SiO_2 catalysts with different Pt loadings

Binding energy analysis showed that the binding energies of Ni^{2+} $2p_{3/2}$ and Ni^{2+} $2p_{1/2}$ gradually decreased with increasing Pt loading. In contrast, the binding energies of Pt^{2+} $4f_{7/2}$ and Pt^{2+} $4f_{5/2}$ slightly increased, as shown in Fig. 5b. These results indicate electron transfer between Pt and NiO_x. During this process, electrons were transferred from Pt to NiO_x at the Pt/NiO_x interface, leading to the formation of electron-deficient $Pt^{\delta+}$ species and corresponding shifts in the XPS binding energies. These results indicate interfacial electronic coupling between Pt and NiO_x, confirming the existence of strong MSI [53, 54]. After sensitivity factor correction, the fitted Pt 4f peak area under identical measurement conditions increased with increasing Pt loading, indicating progressive enrichment of Pt species at the catalyst surface. In contrast, the relative NiO_x related peak area decreased, suggesting that a fraction of the surface

exposed Ni species became covered by Pt species. This coverage may reduce the accessibility of NiO_x surface sites and alter the distribution of Pt/NiO_x interfacial sites, thereby weakening the beneficial contribution of the MSI effect at excessive Pt loadings [55].

The XPS results reveal strong interfacial electronic coupling between Pt and NiO_x, as evidenced by the opposite shifts in the Pt 4f and Ni 2p binding energies. This interfacial charge redistribution effectively modulates the interfacial electronic structure, thereby strengthening the MSI at the Pt/NiO_x interface and enhancing the catalytic performance [33, 56]. However, excessive Pt loading may induce Pt particle aggregation, leading to a reduction in the effective Pt/NiO_x interfacial contact area and thereby weakening the favorable MSI effect [57, 58]. Furthermore, under the high temperature DRM reaction conditions, larger Pt particles readily undergo Ostwald ripening, thereby accelerating catalyst deactivation [24, 59]. Notably, the catalyst with a moderate Pt loading of 4.2wt% exhibits the most balanced interfacial electronic coupling and interface structure, thereby enhancing catalytic activity and stability [33, 40].

3.2.2 DRM activity and stability of Pt/NiO_x-SiO_2 Catalysts with different Pt loadings

As shown in Fig. 6, the catalytic performance of the Pt/NiO_x-SiO_2 series of catalysts varies with the loading of active metals. Specifically, as shown in Fig. 6a and Fig. 6b, the activity of the 0.74wt% Pt/NiO_x-SiO_2 and 0.37wt% Pt/NiO_x-SiO_2 catalysts is lower than that of the 2.1wt% Pt/NiO_x-SiO_2 catalyst. This is likely due to the insufficient number of active interface sites resulting from the lower platinum loading, which leads to a weaker modulation effect of the support structure and consequently poorer catalytic performance [60, 61]. Among all the catalysts investigated, the 4.2wt% Pt/NiO_x-SiO_2 catalyst exhibited the best overall catalytic performance, with an initial CH_4 conversion of approximately 85%, which decreased only slightly to 82.7% after 24 h of DRM reaction, demonstrating excellent short-term stability. To further evaluate its long-term stability, a continuous DRM test for up to 200 h was performed and compared with the 100h stability result of the 2.1wt% Pt/NiO_x-SiO_2 catalyst. As shown in Fig. 6e, the 4.2wt% Pt/NiO_x-SiO_2 catalyst maintained a CH_4 conversion of 81.3% even after 200 h on stream, indicating superior long-term stability. Combined with the TEM characterization results, it is suggested that an appropriate Pt loading establishes a favorable balance between the dispersion of Pt species and the Pt/NiO_x interfacial interaction, thereby effectively suppressing the migration and aggregation of Pt species under high-temperature reaction conditions and consequently enhancing the long-term stability

of the catalyst [62]. At this loading, the Pt component is sufficiently dispersed on the NiO_x surface while maintaining an adequate density of active sites, thereby enhancing catalytic activity while ensuring thermal stability. Although the 6.3wt% Pt/NiO_x-SiO_2 catalyst exhibited higher initial catalytic activity, rapid deactivation was observed during the reaction; 3 h after the start of the reaction, the methane conversion rate dropped to approximately 78%, and the carbon dioxide conversion rate decreased to approximately 65.4%. The reason for its poor stability may lie in the excessive Pt loading, which led to the Ostwald ripening of Pt species, thereby reducing the dispersion of Pt and decreasing the effective Pt/NiO_x interfacial area [62]. At the same time, the structural reconstruction of the spent 6.3wt% Pt/NiO_x-SiO_2 catalyst observed in our XRD analysis further confirmed the instability of the high-loading catalyst during the catalytic reaction.

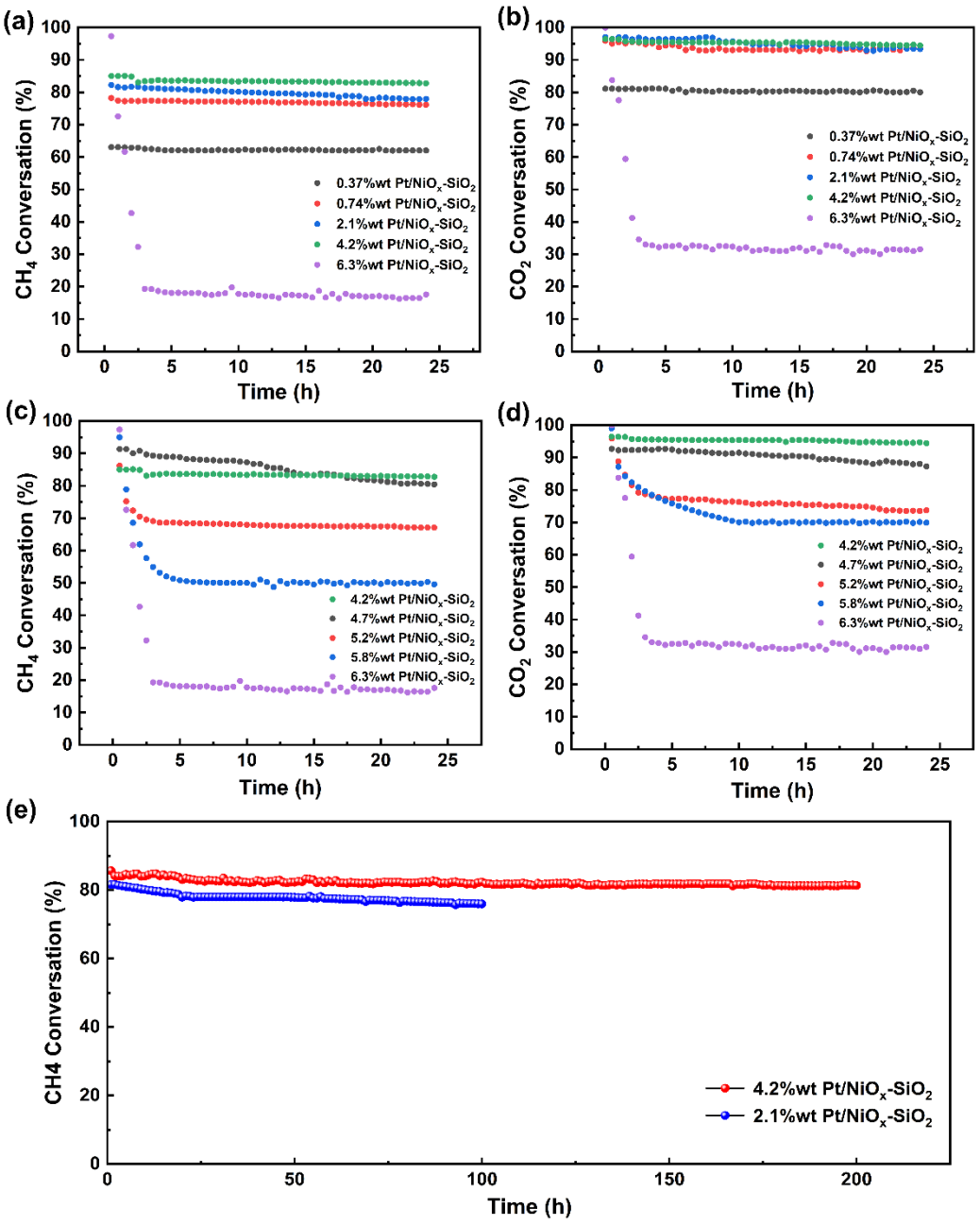


Fig. 6 DRM performance of Pt/NiO_x-SiO_2 catalysts with different Pt loadings. (a) CH_4 and (b) CO_2 conversion over 24 h DRM for catalysts with broad Pt loading range (0.37-6.3wt%); (c) CH_4 and (d) CO_2 conversion over 24 h DRM for catalysts with optimized Pt loading range (4.2-6.3wt%); (e) CH_4 conversion over the 4.2wt% and 2.1wt% Pt/NiO_x-SiO_2 catalysts during 200 and 100 h long-term stability tests

To further elucidate the relationship between rapid catalyst deactivation and Pt loading, additional DRM 24 h tests were conducted at Pt loadings between 4.2 and 6.3wt%. As shown in Fig. 6c and Fig. 6d, our tests revealed that the 4.7wt% Pt/NiO_x-SiO_2 catalyst did not exhibit rapid activity decline;

however, its long-term thermal stability began to show a significant decrease compared to the 4.2wt% Pt/NiO_x-SiO_2 catalyst. In contrast, both 5.2wt% Pt/NiO_x-SiO_2 and 5.8wt% Pt/NiO_x-SiO_2 exhibited varying degrees of rapid activity decline. By comparing the three catalyst groups with different loading levels: 5.2wt% Pt/NiO_x-SiO_2, 5.8wt% Comparison of Pt/NiO_x-SiO_2 and 6.3wt% Pt/NiO_x-SiO_2 reveals that the catalyst with the higher Pt loading undergoes a more pronounced initial decline in activity and exhibits a lower residual activity thereafter. This behavior is likely associated with the higher surface density of Pt species at increased Pt loadings, which enhances the likelihood of Pt migration and aggregation under reaction conditions. This leads to particle growth via the Ostwald ripening mechanism, which in turn reduces the effective specific surface area between Pt and NiO_x and weakens the MSI effect beneficial to catalytic performance.

3.2.3 XRD analysis of fresh and spent Pt/NiO_x-SiO_2 Catalysts with different Pt loadings

The XRD patterns of fresh Pt/NiO_x-SiO_2 catalysts with different loading levels and their corresponding spent catalysts after 24 h of DRM testing were determined. As shown in Fig. 7a and Fig. 7b, all fresh catalysts exhibited a broad diffraction feature near $2\theta = 22°$, which is attributed to the amorphous SiO_2 support. No Pt related diffraction peaks were detected at low Pt loadings, likely because the Pt content was below the XRD detection limit. The absence of distinct NiO_x reflections suggests that the NiO_x species were highly dispersed or poorly crystalline. With increasing Pt loading, the Pt reflections at approximately 39.8° and 46.2°, assigned to the Pt (111) and (200) planes, respectively, became progressively stronger and sharper, indicating increased Pt crystallization and particle growth. At a loading of 4.2wt%, two characteristic diffraction peaks of metallic Ni were observed at approximately 37.2° and 43.3°. The increased NiO_x crystallite size may be attributed to enhanced Pt/NiO_x interactions at higher Pt loadings, which promote the local aggregation and crystallite growth of NiO_x [60]. When the loading was further increased to 5.2 and 6.3wt%, the NiO_x diffraction peaks gradually disappeared, suggesting changes in the dispersion and local structure of NiO_x at higher Pt loadings.

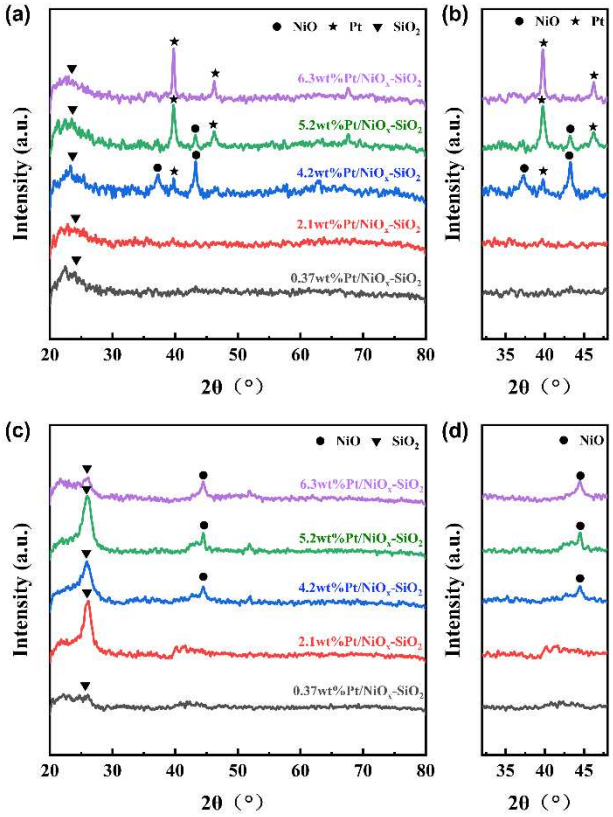


Fig. 7 XRD analysis of Pt/NiO_x-SiO_2 catalysts. (a) XRD patterns of Pt/NiO_x-SiO_2 catalysts with different Pt loadings, (b) enlarged XRD patterns of fresh catalysts between 32 and 48°; (c) XRD patterns of spent catalysts after DRM test at 750 ℃ for 24 h, and (d) enlarged XRD patterns of spent catalysts between 32 and 48°

As shown in Fig. 7c and d, the XRD patterns of the catalysts after 24 h of DRM testing exhibited changes in the broad diffraction feature associated with amorphous SiO_2. For 0.37 wt% Pt/NiO_x-SiO_2, the intensity of this feature decreased after the reaction, suggesting a change in the short-range structural environment of the support. However, because the intensity of an amorphous diffraction feature can also be influenced by sample preparation, background contributions, and data normalization, this change alone does not provide conclusive evidence of support restructuring [63-65]. For the three groups of 2.1wt% Pt/NiO_x-SiO_2, 4.2wt% Pt/NiO_x-SiO_2, and 5.2wt% Pt/NiO_x-SiO_2, the diffraction peaks associated with SiO_2 became relatively sharper, indicating that during the catalytic reaction, the SiO_2 framework may have undergone partial structural rearrangement, and local order was enhanced [66,67]. In contrast, in the 6.3wt% Pt/NiO_x-SiO_2 catalyst, the diffraction peak of amorphous SiO_2 significantly weakened or nearly disappeared. This may be attributed to the extensive coverage of the surface by Pt/NiO_x species,

leading to structural reorganization of the entire catalyst following the DRM reaction [27]. Meanwhile, a distinct diffraction peak centered at approximately 43° was observed after the reaction and can be assigned to the NiO (200) plane. As the Pt loading increased from 4.2 to 6.3wt%, this peak became progressively stronger and sharper, indicating increased crystallization and aggregation of NiO_x species during the reaction. The enhanced NiO crystallization at high Pt loadings may be associated with the migration and redistribution of NiO_x species under DRM conditions, resulting in the formation of larger crystalline NiO domains [68]. This structural evolution could alter the distribution and accessibility of Pt/NiO_x interfacial sites, potentially contributing to the deactivation of catalysts with high Pt loadings [69, 70]. Overall, the XRD results indicate that excessive Pt loading is associated with more pronounced structural evolution under DRM conditions, consistent with the lower stability observed in the activity tests.

The structural evolution observed in XRD testing may be related to the Ostwald ripening process. During this process, NiO_x particles gradually crystallize and migrate to coalesce into larger crystalline domains, reducing the effective surface area of the Pt/NiO_x catalyst. This makes Pt particles more susceptible to Ostwald ripening under the high-temperature reaction conditions of DRM, resulting in accelerated deactivation of high-loading catalysts [71].

The XRD, XPS, and DRM activity results indicate that an appropriate Pt loading is important for balancing Pt dispersion, the Pt/NiO_x interfacial structure, and the MSI effect. Insufficient Pt loading leads to a limited number of active sites at the Pt/NiO_x interface, while excessive loading causes particle growth and Ostwald ripening, resulting in a deterioration of the Pt/NiO_x interface performance. Among all catalysts, the 4.2wt% Pt/NiO_x-SiO_2 catalyst achieved the optimal balance between structural stability and electronic interactions, thereby exhibiting superior catalytic performance.

3.3 Structural evolution and deactivation mechanism of high Pt loading Pt/NiO_x-SiO_2 catalyst during dry reforming of methane reaction

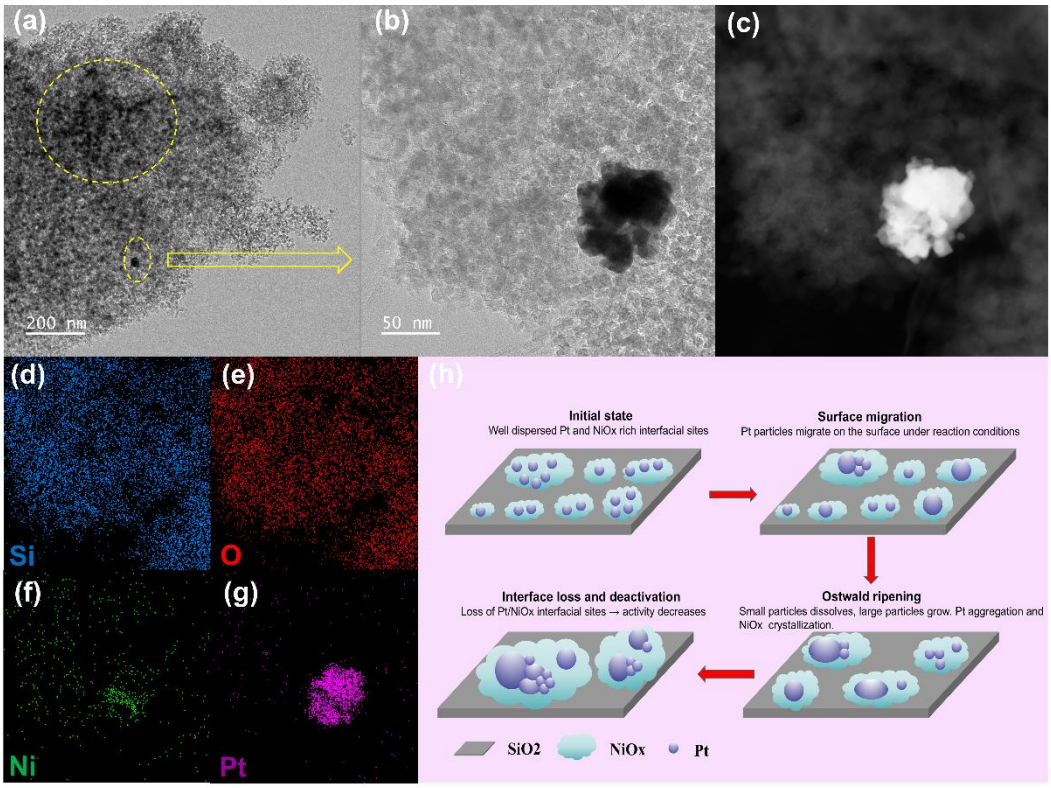


Fig. 9 Structural evolution and deactivation mechanism of high-loading Pt/NiO_x-SiO_2 catalyst during DRM reaction. (a) TEM image, (b) enlarged TEM image, (c) HAADF-STEM image, and (d–g) STEM-EDS elemental mappings of Si, O, Ni, and Pt for the spent high-loading Pt/NiO_x-SiO_2 catalyst after DRM reaction. (h) Schematic illustration of the proposed structural evolution and deactivation mechanism, involving Pt migration, Ostwald ripening, Pt aggregation, NiO_x crystallization, and loss of Pt-NiO_x interfacial active sites under DRM conditions.

To further investigate the structural evolution of the high Pt loading catalyst during the DRM reaction, the spent 6.3wt% Pt/NiO_x-SiO_2 catalyst after DRM testing was characterized by TEM, HAADF-STEM, and STEM-EDS mapping. As shown in Fig. 8(a-b), obvious Pt-enriched regions were observed on the catalyst surface after the DRM reaction at 750 °C for 24 h. Compared with the fresh catalyst, the dispersion state of Pt species was significantly altered after reaction. The HAADF-STEM image (Fig. 8c) revealed enhanced bright contrast regions, indicating that Pt species underwent surface migration and partial aggregation under high-temperature reaction conditions. Furthermore, the STEM-EDS mapping results (Fig. 8(d-g)) demonstrated that Pt elements were mainly concentrated in localized

regions after reaction, accompanied by the redistribution of Ni species, suggesting that both Pt species and NiO_x domains underwent structural evolution during the high-temperature DRM process.

The aggregation of active metal species observed by TEM was consistent with the sintering process induced by Ostwald ripening under high-temperature conditions. Moreover, owing to the unique structural characteristics of SANIs-like catalysts, in which oxide islands are dispersed on the SiO_2 support, the migration and aggregation of Pt species may further influence the stability and distribution of NiO_x islands on the SiO_2 surface.

Based on the XPS and XRD characterization results, a proposed structural evolution and deactivation mechanism of the high Pt loading Pt/NiO_x-SiO_2 catalyst is illustrated in Fig. 8h. During the high-temperature DRM reaction, Pt species initially migrated and underwent particle growth on the NiO_x surface, while NiO_x species may also experience migration and crystallization, resulting in the formation of larger NiO_x crystallites. The synergistic effects of Pt aggregation and NiO_x structural reconstruction gradually reduced the number of accessible Pt/NiO_x interfacial active sites and caused partial coverage of active regions, ultimately leading to catalyst deactivation.

4 Conclusion

Inspired by the concept of SANIs, this study successfully synthesized a series of oxide-supported Pt catalysts via the LEA method and investigated the role of MSI in DRM catalysis. TEM, HRTEM, and STEM-EDS mapping analyses confirmed the highly dispersed distribution of Pt species and the formation of Pt/NiO_x interfacial structures in the Pt/NiO_x-SiO_2 catalyst. Furthermore, catalysts with different Pt loadings were synthesized to investigate the effects of oxide support type and Pt loading on the active metal-support interface, catalytic activity, and thermal stability. BET results indicated that the differences in catalytic performance were not primarily related to surface textural properties but were mainly associated with the MSI between Pt species and oxide supports.

Among the various oxide support catalysts studied, Pt/NiO_x-SiO_2 exhibited the strongest Pt/NiO_x interaction, resulting in superior DRM catalytic activity and stability. XPS analysis revealed significant electronic interactions between Pt and NiO_x. The 24 h DRM activity test and 100 h DRM stability test demonstrated the excellent catalytic performance of Pt/NiO_x-SiO_2, while H_2-TPR results confirmed the

strong interactions at the Pt/NiO_x interface. In contrast, other oxide support catalysts exhibited relatively weak interfacial interactions and poor catalytic performance.

Further optimization of the Pt loading on Pt/NiO_x-SiO_2 revealed that the dispersion state of Pt species and the density of Pt/NiO_x interfacial sites significantly influenced the catalytic performance. The catalyst with a Pt loading of 4.2wt% exhibited the most balanced interfacial structure and delivered the optimal DRM performance, achieving a CH_4 conversion of 85% and maintaining 81.3% after 200 h of continuous operation. In contrast, at excessively high Pt loading, Pt aggregation and Ostwald ripening occurred under the high-temperature DRM conditions, accompanied by enhanced crystallization and migration of NiO_x species. These structural changes induced the reconstruction of the Pt/NiO_x interface, weakened the beneficial MSI effect, and ultimately accelerated catalyst deactivation.

The above results indicate that the synergistic regulation of MSI and the distribution of active metal interfaces plays a crucial role in enhancing the catalytic activity and stability of SANIs-inspired catalysts in the DRM process. This study provides a feasible strategy for designing highly stable DRM catalysts through interface structural engineering.

References

[1] Y. Meng, Y. Tuo, Y. Xue, X. Yan, Z. Luo, Q. Yang, S. Chernyshikhin, Y. Yan, M. Lin, Y. Zhao, X. Meng, Carbon Energy 8, e70127 (2026). https://doi.org/10.1002/cey2.70127

[2] Z. Alipour, V. Babu Borugadda, H. Wang, A.K. Dalai, Chem. Eng. J. 452, 139416 (2023). https://doi.org/10.1016/j.cej.2022.139416

[3] C. Sampson, T. Masuda, T. Horiguchi, S. Ichiguchi, H. Sampei, H. Matsubara, S. Itagaki, G. Inoue, Y. Sekine, ACS Catal. 15, 12885-12896 (2025). https://doi.org/10.1021/acscatal.5c03126

[4] M. Akri, M. El Doukkali, Mater. Today Chem. 45, 102673 (2025). https://doi.org/10.1016/j.mtchem.2025.102673

[5] Z. Li, B. Li, Q. Li, Adv. Mater. 35, 2211103 (2023). https://doi.org/10.1002/adma.202211103

[6] X. Li, X.I. Pereira-Hernández, Y. Chen, J. Xu, J. Zhao, C.W. Pao, C.Y. Fang, J. Zeng, Y. Wang, B.C. Gates, J. Liu, Nature 611, 284-288 (2022). https://doi.org/10.1038/s41586-022-05251-6

[7] Y. Long, L. Gao, Y. Zhang, W.-L. Ong, H. Zhang, J. Yan, RSC Adv. 15, 10896-10901 (2025). https://doi.org/10.1039/d5ra00007f

[8] Y. Wu, J. Liu, J. Liu, Z. Jiang, M. Tian, J. Wang, F. Dang, C. Ai, R. Albilali, C. He, Chem. Eng. J. 538, 176790 (2026). https://doi.org/10.1016/j.cej.2026.176790

[9] P.N. Plessow, C.T. Campbell, ACS Catal. 12, 2302-2308 (2022). https://doi.org/10.1021/acscatal.1c04633

[10] C.T. Campbell, Z. Mao, ACS Catal. 7, 8460-8466 (2017). https://doi.org/10.1021/acscatal.7b03090

[11] T. Wang, J. Hu, R. Ouyang, Y. Wang, Y. Huang, S. Hu, W.X. Li, Science 386, 915-920 (2024). https://doi.org/10.1126/science.adp6034

[12] Y. Gangarajula, F. Hong, Q. Li, X. Jiang, W. Liu, M. Akri, Y. Su, Y. Zhang, L. Li, B. Qiao, Appl. Catal. B Environ. Energy 343, 123503 (2024). https://doi.org/10.1016/j.apcatb.2023.123503

[13] X. Feng, Y. Zhao, S. Liu, K. Wang, B. Liu, Q. Zhang, H. Wang, Y. Zhao, J. Liu, P. Zhang, L. Gao, Fuel 358, 130029 (2024). https://doi.org/10.1016/j.fuel.2023.130029

[14] Y. Xu, Z. An, X. Yu, J. Yao, Q. Lv, H. Yang, Z. Lv, H. Guo, Q. Jiang, W. Liu, L. Wu, L. Tan, Y. Dai, Y. Tang, J. Catal. 427, 115094 (2023). https://doi.org/10.1016/j.jcat.2023.08.010

[15] C. Han, S. Zhang, H. Zhang, Y. Dong, P. Yao, Y. Du, P. Song, X. Gong, W. Xu, eScience 4, 100269 (2024). https://doi.org/10.1016/j.esci.2024.100269

[16] H. Tang, F. Dong, S. Chen, J. Huang, F. Hong, Y. Su, G. Bai, B. Qiao, ACS Catal. 14, acscatal.4c03421 (2024). https://doi.org/10.1021/acscatal.4c03421

[17] X. Sui, L. Zhang, J. Li, K. Doyle-Davis, R. Li, Z. Wang, X. Sun, J. Mater. Chem. A 8, 16582-16589 (2020). https://doi.org/10.1039/d0ta02681f

[18] J. Wei, H. Tang, L. Sheng, R. Wang, M. Fan, J. Wan, Y. Wu, Z. Zhang, S. Zhou, J. Zeng, Nat. Commun. 15, 559 (2024). https://doi.org/10.1038/s41467-024-44815-0

[19] J. Zhang, D. Zhu, J. Yan, C.A. Wang, Nat. Commun. 12, 6665 (2021). https://doi.org/10.1038/s41467-021-27000-5

[20] S. Hu, W.X. Li, Science 374, 1360-1365 (2021). https://doi.org/10.1126/science.abi9828

[21] E.M. Dietze, F. Abild-Pedersen, P.N. Plessow, J. Phys. Chem. C 122, 26563-26569 (2018). https://doi.org/10.1021/acs.jpcc.8b09303

[22] Q. Liu, Y. Fang, X. Xiong, W. Xu, J. Cui, Angew. Chem. Int. Ed. 63, e202320095 (2024). https://doi.org/10.1002/anie.202320095

[23] T.P. Doan-Nguyen, S. Jiang, K. Koynov, K. Landfester, D. Crespy, Angew. Chem. Int. Ed. 60,

18094-18102 (2021). https://doi.org/10.1002/anie.202103444
[24] J.W. Han, J.S. Park, M.S. Choi, H. Lee, Appl. Catal. B Environ. Energy 203, 625-632 (2017). https://doi.org/10.1016/j.apcatb.2016.10.069
[25] J. Huang, Y. Zhang, J. Chen, Z. Zhang, C. Zhang, C. Huang, L. Fei, Chem. Sci. 15, 14521-14530 (2024). https://doi.org/10.1039/d4sc03284e
[26] M. Gan, J. Huang, X. Li, M. Li, Z. Zhang, Z. Yang, C. Zhang, P. Yang, X. Gan, C. Lu, X. Yang, L. Fei, C. Huang, J. Mater. Chem. A 12, 29174-29183 (2024). https://doi.org/10.1039/d4ta05822d
[27] F. Yu, X. Tao, H. Yu, T. Zhao, M. Li, L. Liu, H. Wang, Chem. Eng. J. 504, 158725 (2025). https://doi.org/10.1016/j.cej.2024.158725
[28] J. Loeb, J. Gen. Physiol. 1, 237-254 (1918). https://doi.org/10.1085/jgp.1.2.237
[29] S. Salgın, U. Salgın, S. Bahadır, Int. J. Electrochem. Sci. 7, 12404-12414 (2012). https://doi.org/10.1016/s1452-3981(23)16554-0
[30] M. Kosmulski, Adv. Colloid Interface Sci. 296, 102519 (2021). https://doi.org/10.1016/j.cis.2021.102519
[31] L. Wang, J. Jin, C. Li, W. Li, M. Miao, L. Yuan, ACS Nano 19, 32981-32991 (2025). https://doi.org/10.1021/acsnano.5c12941
[32] J. Wang, J. Lucas, H. Nakashima, I. Ogino, K.M. Dooley, O.M. Gazit, Appl. Catal. B Environ. Energy 366, 125004 (2025). https://doi.org/10.1016/j.apcatb.2024.125004
[33] T. Zhou, X. Li, J. Zhao, L. Luo, Y. Wang, Z. Xiao, S. Hu, R. Wang, Z. Zhao, C. Liu, W. Wu, H. Li, Z. Zhang, L. Zhao, H. Yan, J. Zeng, Nat. Mater. 24, 891-899 (2025). https://doi.org/10.1038/s41563-025-02134-9
[34] M.C. Biesinger, B.P. Payne, A.P. Grosvenor, L.W.M. Lau, A.R. Gerson, R.S.C. Smart, Appl. Surf. Sci. 257, 2717-2730 (2011). https://doi.org/10.1016/j.apsusc.2010.10.051
[35] H. Liu, G. Wei, Z. Xu, P. Liu, Y. Li, Appl. Surf. Sci. 389, 438-446 (2016). https://doi.org/10.1016/j.apsusc.2016.07.146
[36] Z. Fu, J. Hu, W. Hu, S. Yang, Y. Luo, Appl. Surf. Sci. 441, 1048-1056 (2018). https://doi.org/10.1016/j.apsusc.2018.02.114
[37] O. Lupan, G.A. Emelchenko, V.V. Ursaki, G. Chai, A.N. Redkin, A.N. Gruzintsev, I.M. Tiginyanu, L. Chow, L.K. Ono, B. Roldan Cuenya, H. Heinrich, E.E. Yakimov, Mater. Res. Bull. 45, 1026-1032 (2010). https://doi.org/10.1016/j.materresbull.2010.03.027
[38] J. Halim, K.M. Cook, M. Naguib, P. Eklund, Y. Gogotsi, J. Rosen, M.W. Barsoum, Appl. Surf. Sci. 362, 406-417 (2016). https://doi.org/10.1016/j.apsusc.2015.11.089
[39] S. Zhao, J. Lin, W. Gong, A. Xu, X. Li, Y. Qiu, Sep. Purif. Technol. 332, 125864 (2024). https://doi.org/10.1016/j.seppur.2023.125864
[40] X. Hao, S. Wu, X. Lv, J. Chen, H. Jia, Sep. Purif. Technol. 358, 130266 (2025). https://doi.org/10.1016/j.seppur.2024.130266
[41] D. Liu, F. Jiang, Q. Zhang, W.H. Huang, Y. Zheng, M. Chen, L. Wu, R. Qin, M. Wang, S. Zhang, L. Chen, K. Yan, L. Zhou, Y. Zhao, L. Gu, G. Chen, ACS Nano 18, 34671-34682 (2024). https://doi.org/10.1021/acsnano.4c10030
[42] X. Chen, Z. Jia, Z. Liu, X. Wang, M. Liang, RSC Adv. 13, 3255-3264 (2023). https://doi.org/10.1039/d2ra07650k
[43] Y. Yang, Z. Chai, X. Qin, Z. Zhang, A. Muhetaer, C. Wang, H. Huang, C. Yang, D. Ma, Q. Li, D. Xu, Angew. Chem. Int. Ed. 61, e202200567 (2022). https://doi.org/10.1002/anie.202200567
[44] C.T. Campbell, Nat. Chem. 4, 597-598 (2012). https://doi.org/10.1038/nchem.1412

[45] H. Xiong, Z. Dai, C. Fu, X. Ji, Y. Dong, M. Ge, R. Long, Y. Bi, Y. Xiong, J. Am. Chem. Soc. 147, 38204-38214 (2025). https://doi.org/10.1021/jacs.5c10497

[46] J. Li, L. Zhang, X. An, K. Feng, X. Wang, J. He, Y. Huang, J. Liu, L. Zhang, B. Yan, C. Li, L. He, Angew. Chem. Int. Ed. 63, e202407025 (2024). https://doi.org/10.1002/anie.202407025

[47] S.B. Trung Tran, H.S. Choi, S.Y. Oh, S.Y. Moon, J.Y. Park, RSC Adv. 8, 21528-21533 (2018). https://doi.org/10.1039/c8ra03664k

[48] H. Wang, T.D. Nguyen, G. Tsilomelekis, Catal. Sci. Technol. 13, 2360-2369 (2023). https://doi.org/10.1039/d2cy01563c

[49] Q. Song, R. Ran, X. Wu, Z. Si, D. Weng, J. CO2 Util. 68, 102387 (2023). https://doi.org/10.1016/j.jcou.2022.102387

[50] Y. Zhang, S. Li, Y. Fu, L. Zheng, H. Li, W. Kong, B. Pan, J. Li, J. Zhang, Y. Sun, Appl. Catal. B Environ. Energy 350, 123903 (2024). https://doi.org/10.1016/j.apcatb.2024.123903

[51] P. Yang, X. Wei, L. Zhang, S. Dong, W. Cao, D. Ma, Y. Ouyang, Molecules 28, 2995 (2023). https://doi.org/10.3390/molecules28072995

[52] A.A. Saraev, A.Y. Kurenkova, A.V. Zhurenok, E.Y. Gerasimov, E.A. Kozlova, Catalysts 13, 273 (2023). https://doi.org/10.3390/catal13020273

[53] L. Huang, N. Wang, M. Qi, Z. Liu, Z. Xu, Q. Zhang, Z. Shu, S. Shan, Y. Bian, J. Chen, Y. Jiao, Int. J. Hydrog. Energy 88, 1217-1225 (2024). https://doi.org/10.1016/j.ijhydene.2024.09.194

[54] G. Wu, Y. Liu, J. Wang, Acc. Chem. Res. 56, 911-923 (2023). https://doi.org/10.1021/acs.accounts.2c00727

[55] A.R.M. Alghamdi, M. Yanagida, Y. Shirai, G.G. Andersson, K. Miyano, ACS Omega 7, 12147-12157 (2022). https://doi.org/10.1021/acsomega.2c00509

[56] E. Cui, Q. Li, X. Wang, N. Xu, F. Zhang, G. Hou, M. Xie, Z. Wang, X. Yang, Y. Zhang, Appl. Catal. B Environ. Energy 329, 122560 (2023). https://doi.org/10.1016/j.apcatb.2023.122560

[57] Z. Lu, G. Sun, S. Chen, D. Fu, C. Pei, J. Gong, Chem. Eng. Sci. 297, 120304 (2024). https://doi.org/10.1016/j.ces.2024.120304

[58] F. Qi, J. Peng, Z. Liang, J. Guo, J. Liu, T. Fang, H. Mao, Environ. Sci. Ecotechnol. 22, 100443 (2024). https://doi.org/10.1016/j.ese.2024.100443

[59] W.L. Noorduin, E. Vlieg, R.M. Kellogg, B. Kaptein, Angew. Chem. Int. Ed. 48, 9600-9606 (2009). https://doi.org/10.1002/anie.200905215

[60] F. Wang, Z. Zheng, D. Wu, H. Wan, G. Chen, N. Zhang, X. Liu, R. Ma, Chem. Sci. 15, 10172-10181 (2024). https://doi.org/10.1039/d4sc00454j

[61] Y. Ou, S. Li, Z. Wang, X. Xu, X. Guo, Q. Chen, T. Sun, Y. Zhu, Mater. Today Nano 32, 100713 (2025). https://doi.org/10.1016/j.mtnano.2025.100713

[62] D.G. Araiza, D.G. Arcos, A. Gómez-Cortés, G. Díaz, Catal. Today 360, 46-54 (2021). https://doi.org/10.1016/j.cattod.2019.06.018

[63] G. Lucovsky, J.C. Phillips, Nanoscale Res. Lett. 5, 550-558 (2010). https://doi.org/10.1007/s11671-009-9520-6

[64] W. Jin, R.K. Kalia, P. Vashishta, J.P. Rino, Phys. Rev. Lett. 71, 3146-3149 (1993). https://doi.org/10.1103/physrevlett.71.3146

[65] A.S. D'Souza, C.G. Pantano, J. Am. Ceram. Soc. 82, 1289-1293 (1999). https://doi.org/10.1111/j.1151-2916.1999.tb01909.x

[66] M. Shiga, A. Hirata, Y. Onodera, H. Masai, Commun. Mater. 4, 91 (2023). https://doi.org/10.1038/s43246-023-00416-w

[67] K. Kobayashi, M. Okumura, H. Nakamura, M. Itakura, M. Machida, S. Urata, K. Suzuya, Sci. Rep. 13, 18721 (2023). https://doi.org/10.1038/s41598-023-44732-0
[68] J. Kim, W.H. Park, W.H. Doh, S.W. Lee, M.C. Noh, J.J. Gallet, F. Bournel, H. Kondoh, K. Mase, Y. Jung, B.S. Mun, J.Y. Park, Sci. Adv. 4, eaat3151 (2018). https://doi.org/10.1126/sciadv.aat3151
[69] Z. Luo, G. Zhao, H. Pan, W. Sun, Adv. Energy Mater. 12, 2201395 (2022). https://doi.org/10.1002/aenm.202201395
[70] T.S. Kim, J. Kim, H.C. Song, D. Kim, B. Jeong, J. Lee, J.W. Shin, R. Ryoo, J.Y. Park, ACS Catal. 10, 10459-10467 (2020). https://doi.org/10.1021/acscatal.0c02467
[71] S.D.P. Fielden, Aggregate 6, e70116 (2025). https://doi.org/10.1002/agt2.70116

List of abbreviations

Abbreviation	**Full name**
AlO_x	Aluminum oxide
BET	Brunauer–Emmett–Teller
CH_4	Methane
CO	Carbon monoxide
CO_2	Carbon dioxide
CoO_x	Cobalt oxide
CrO_x	Chromium oxide
DRM	Dry Reforming of Methane
FID	Flame Ionization Detector
GC	Gas Chromatograph
GHSV	Gas Hourly Space Velocity
H_2	Hydrogen
H_2-TPR	Hydrogen Temperature-Programmed Reduction
HRTEM	High-Resolution Transmission Electron Microscopy
HAADF-STEM	High-Angle Annular Dark-Field Scanning Transmission Electron Microscopy
LEA	Liquid-phase Electrostatic Adsorption
MSI	Metal-Support Interaction

NiO_x	Nickel oxide
N_2	Nitrogen
Pt	Platinum
SANIs	Single-Atom Nano-Islands
SiO_2	Silicon dioxide
STEM-EDS	Scanning Transmission Electron Microscopy–Energy Dispersive X-ray Spectroscopy
TEM	Transmission Electron Microscopy
TCD	Thermal Conductivity Detector
XPS	X-ray Photoelectron Spectroscopy
XRD	X-ray Diffraction
ZnO_x	Zinc oxide

Supplementary Files

This is a list of supplementary files associated with this preprint. Click to download.

- Supplementarymaterial.docx